Supplementary Material for

Anomalous Above-Gap Photoexcitations and Optical Signatures of Localized Charge Puddles in Monolayer Molybdenum Disulfide

Nicholas J. Borys[1,2,*], Edward S. Barnard[1,2], Shiyuan Gao[3], Kaiyuan Yao[1], Wei Bao[1,2,4], Alexander Buyanin[2], Yingjie Zhang[2], Sefaattin Tongay[4,5], Changhyun Ko[4], Joonki Suh[4], Alexander Weber-Bargioni[1,2], Junqiao Wu[2,4], Li Yang[3], and P. James Schuck[1,2,†]

[1] Molecular Foundry, [2] Materials Sciences Division, Lawrence Berkeley National Laboratory, Berkeley, CA 94720, USA

[3] Department of Physics, Washington University in St. Louis, St. Louis, MO 63130, USA

[4] Department of Materials Science and Engineering, University of California Berkeley, Berkeley, CA 94720, USA

[5] Department of Materials Science and Engineering, Arizona State University, Tempe, AZ, 85287, USA

[*] njborys@lbl.gov

[†] pjschuck@lbl.gov

1. Effects of thin film interference on the PLE spectrum of monolayer MoS_2

Thin film interference effects from the underlying substrate can dramatically effect the apparent PLE spectrum. Figure S1a shows the PLE spectrum of a single flake of monolayer MoS_2 on top of a Si substrate that is capped with a 300 nm thick layer of SiO_2. The raw PLE spectrum (light gray curve) decreases with increasing excitation energy, a trend which is in stark contrast to what is observed for monolayer MoS_2 on a Si substrate capped with a 100 nm thick SiO_2 layer (cf., Fig. 1 of the main text). In Figure S1b, a simple thin film model is presented where the interference effects are approximated by summing the intensity of the reflected (from the Si/SiO_2 and SiO_2/air interfaces) and incident radiation at a distance of 0.35 nm above the surface. The intensity of the reflected beams and their relative phase differences are calculated using the appropriate Fresnel equations and approximate wavelength-independent indices of refraction (n_{SiO2} = 1.46; n_{air}=1.0; n_{Si} = 4.13). To account for these added interference effects, the raw emission intensity (Fig. S1a; gray curve) is divided by the normalized excitation intensity (Fig. S1b; blue curve). By using this simple model to account for the interference effects, the corrected PLE spectra (Fig. S1a; black curve) exhibits the same increase in excitation with increasing photon energy as observed in the main text. We note that this model neglects non-normal angles of incidences, as well as the effect of the monolayer MoS_2. However, despite these simplifications, with this correction to the PLE data, the agreement between the PLE spectra of monolayer MoS_2 on SiO_2/Si substrates with different oxide thicknesses as well as on sapphire is significantly improved, indicating that this is a decent approximation to account for such effects.

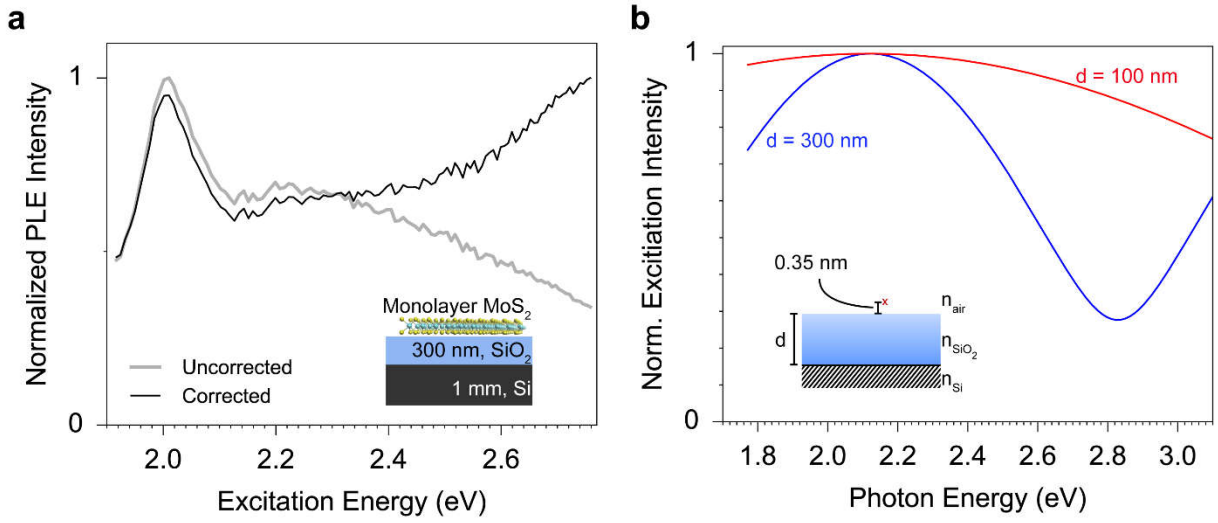

Figure S1 – Effect of thin film interference on the PLE spectrum of monolayer MoS_2. (a) The corrected (black curve) and uncorrected, raw (gray curve) PLE spectra. (b) Normalized excitation intensity over the PLE excitation range for a point 0.35 nm above the SiO2/Si substrate taking into account the interference between the incident and reflected radiation from dielectric interfaces.

2. Observation of photodegredation in monolayer MoS_2

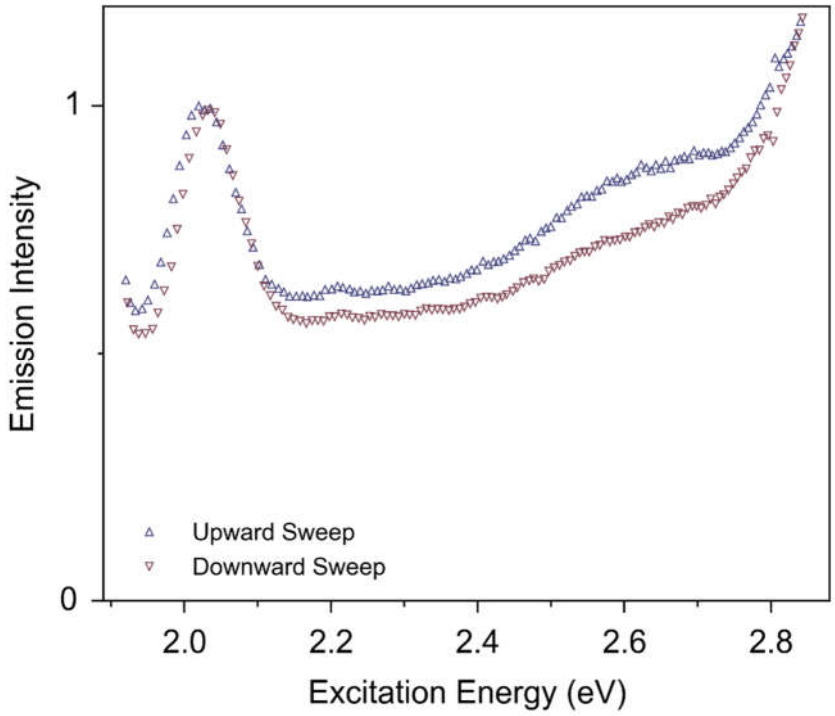

Figure S2 – Photodegredation over up and down sweeps of excitation energy. For all measurements presented in the manuscript, the excitation energy was scanned from low energy to high energy and then back to low energy. As can be seen in this example, the downward scan exhibits a reduced intensity indicating the presence of photodegredation processes, which we found to intensify with increased excitation density as well as increased exposure due to longer integration times. Despite the photodegredation observed here, all of the main spectral features discussed in the manuscript remain, but under less ideal experimental conditions (such as increased integration times), the high-energy part of PLE spectrum could be found to be artificially significantly lower in intensity due to these effects. Preliminary observations indicate that the higher excitation energy induces more photodegredation than at lower energies.

3. Comparison of absorption and PLE spectrum of monolayer MoS_2 on a sapphire substrate

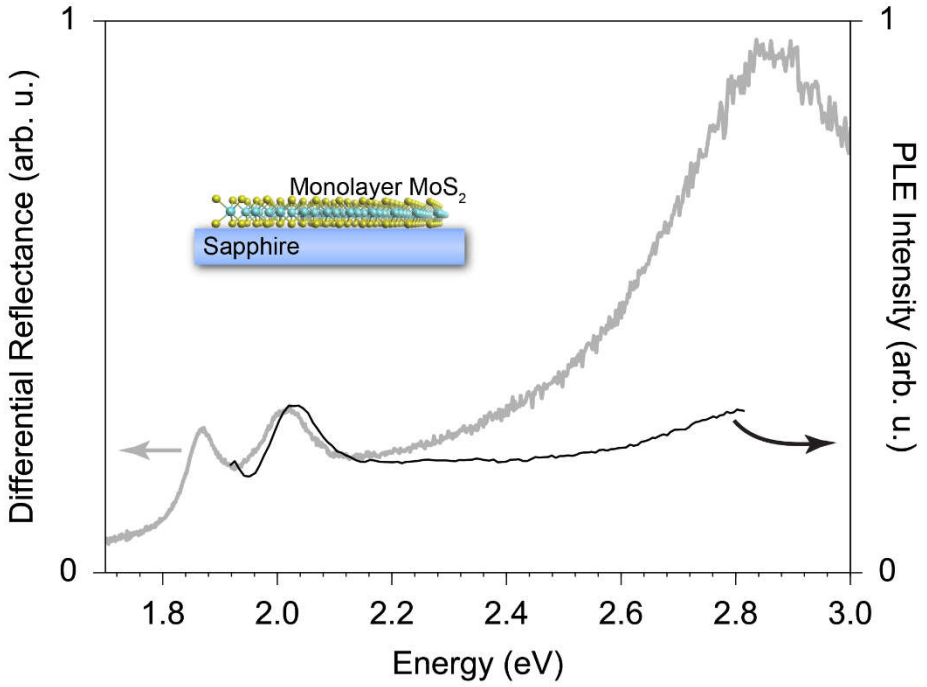

Figure S3 – Differential reflectance and PLE spectra of monolayer MoS_2 on a transparent sapphire substrate. The differential reflectance (gray curve) is the normalized difference in reflectance between the air/MoS_2 interface and the air/sapphire interface: $\Delta R = (R_{sapphire} - R_{MoS2})/R_{sapphire}$. Because thin film interference effects are negligible in this substrate configuration, the spectral from of the differential reflectance closely traces the absorption spectrum. In the absence of interference effects, the PLE spectrum exhibits an increase with increasing excitation energy similar to the corrected PLE spectra on the SiO_2/Si substrates.

4. Derivative analysis of PLE spectrum

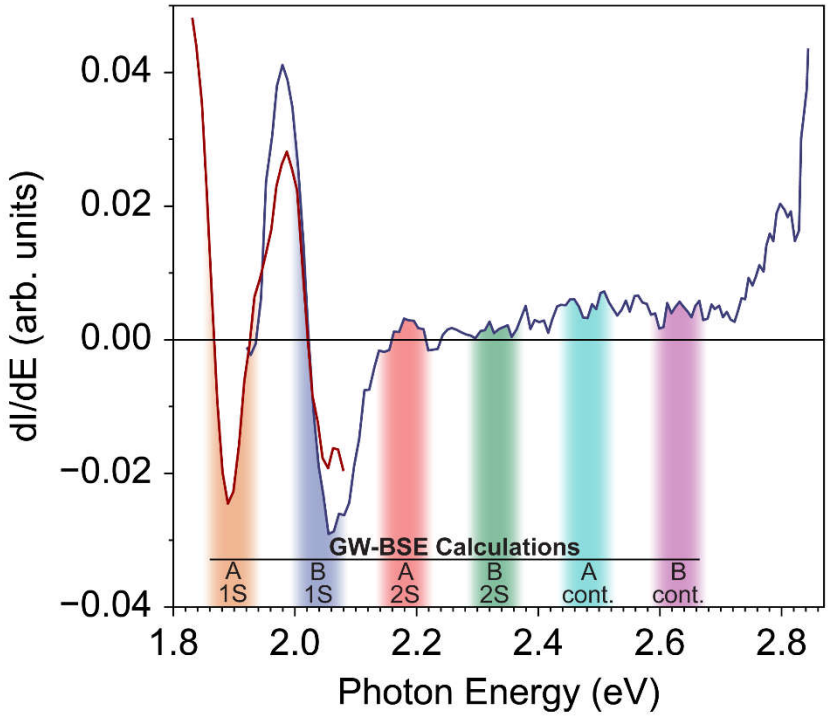

Figure S4 –Derivative analysis of the PLE spectrum of ML-MoS_2. The derivative of the smoothed PLE spectrum presented in Figure 1 of the main text is shown. Zero-crossings are observed at the peak positions of the 1S states of the A and B excitons as well as for the 2S state of the A exciton. As in the PLE spectrum, a feature corresponding to the a peak for the 2S state of the B exciton is not observed, but at 2.48 eV, the subtle changes in the slope are seen by corresponding changes in the derivative.

5. Direct Comparison of PLE spectra reported in this work

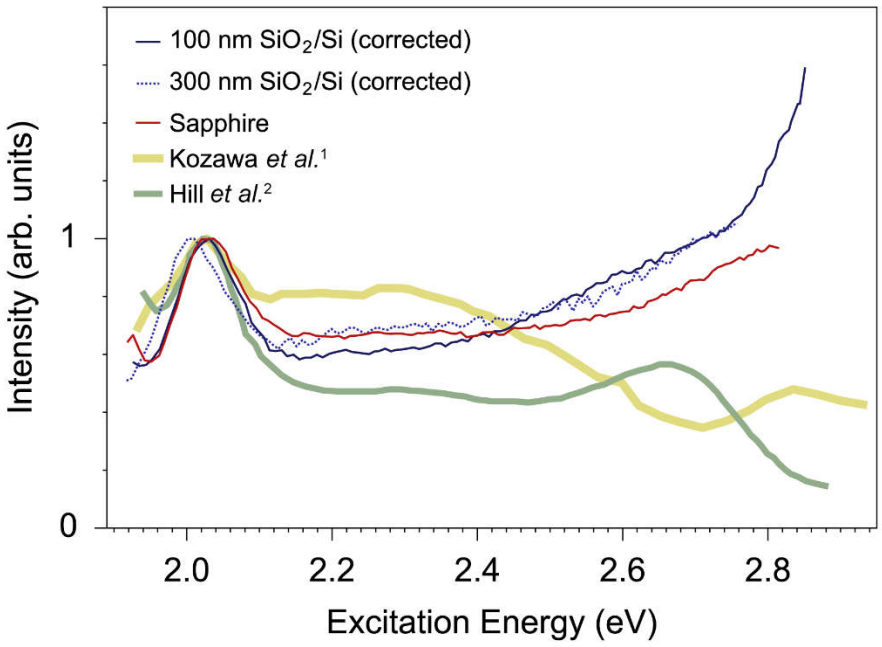

Figure S5 – Direct comparison of PLE spectra of monolayer MoS_2. The corrected PLE spectra of monolayer MoS_2 on a SiO_2/Si substrate with 100 nm (blue line) and 300 nm (dashed blue line) thick oxide layers are compared to that on sapphire (red line) as well as to the previous PLE spectra published by Kozawa *et al.*[1] (light yellow line) and Hill *et al.*[2] (light green line). All spectra are normalized to the B exciton resonance at ~2.03. Among the samples investigated in this study, the increase of the PLE towards higher energy was consistently observed and similar in extent. Unfortunately, technical issues with our laser prevented reaching excitation at energies larger than 2.8 eV for some of the measurements shown, but we anticipate the same increase in all of the samples. In contrast, the previously reported PLE spectra decrease in intensity towards higher energies, which may be due to a combination of varying quality and optoelectronic properties between samples, uncorrected thin-film interference effects, PL degradation at higher excitation energies and excitation in a sublinear regime at the higher excitation energies.

6. Qualitative demonstration of the role of linewidth broadening in the prominence of the higher-energy exciton resonances

The linear absorption of the A and B excitons of monolayer MoS_2 is analytically treated by Bergahäuser *et al.*[3], predicting both the energies and oscillator strengths of the allowed optical transitions which lead up to the quasiparticle bandgap. Direct comparison of our experimental PLE spectrum to the predicted excitonic absorption spectrum of monolayer MoS_2 on an SiO_2 substrate reveals agreement on the energetic positions of the 1S states and the quasiparticle bandgaps of the A and B excitons, as well as the 2S state of the A exciton. In the theoretical analysis by Bergahäuser *et al.*[3], a phenomenological broadening of 50 meV is applied to all exciton states. However, as noted in the main text of this work, the linewidth of the B exciton is larger than that of the A exciton. In this section, we qualitatively estimate the effect of this broadening on the spectrum reported by Bergahäuser *et al.*[3] and demonstrate how the larger linewidth of the B exciton can diminish the prominence of its higher-energy states in the PLE spectrum.

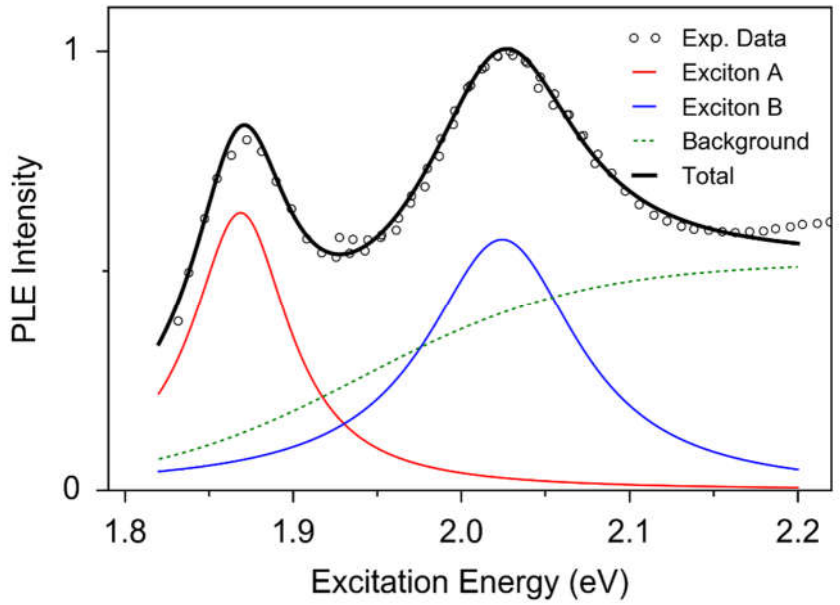

Figure S6 – Linewidth of the excitation resonances of the 1S states of the A and B excitons. A fit (described below) to the experimental PLE spectrum in Figure 1 of the main text yields linewidths of 70 meV and 110 meV for the room temperature 1S states of the A and B excitons, respectively.

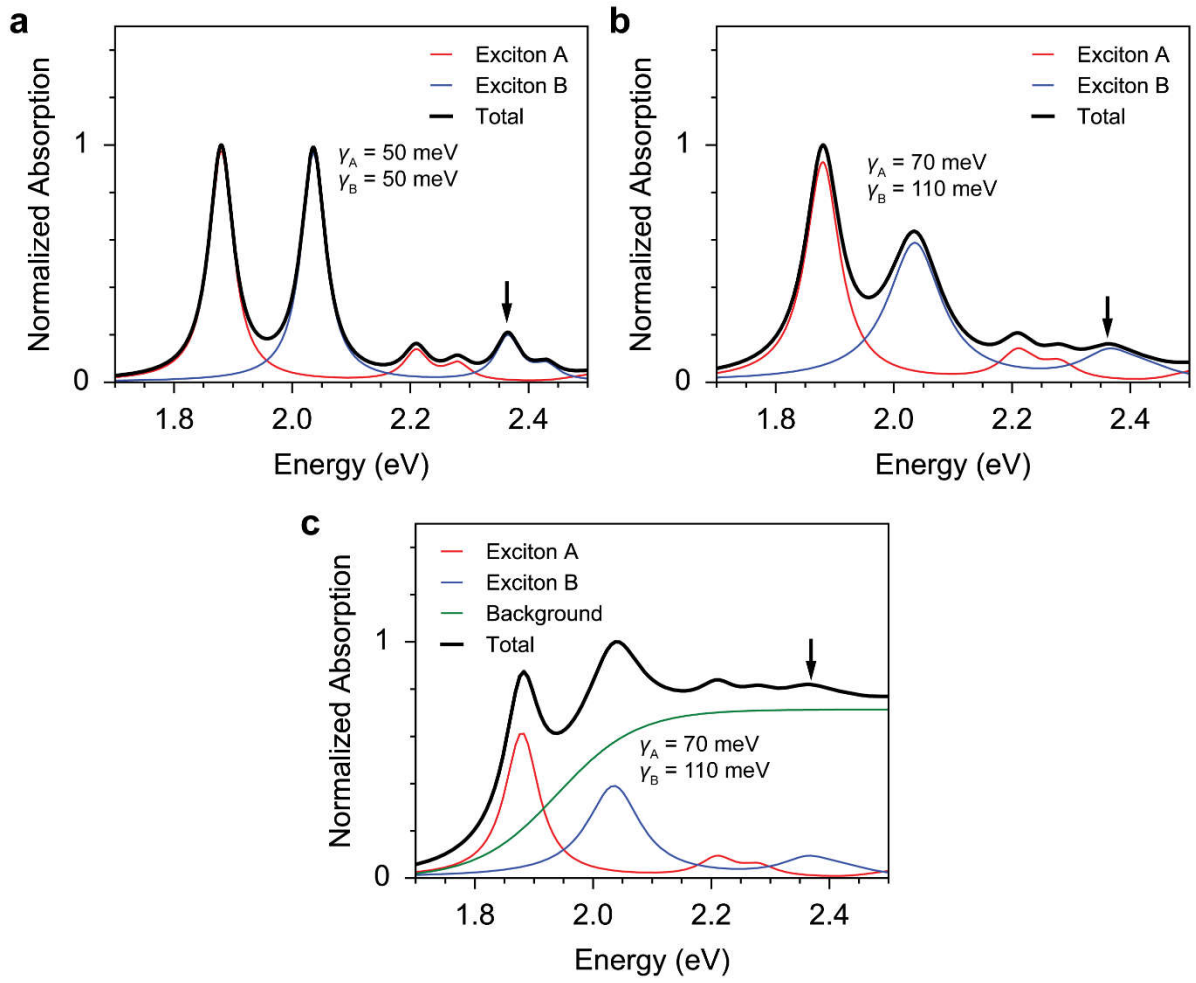

Figure S7 – The effects of broadening on model absorption spectra for the A and B excitons of monolayer MoS_2. a) Reproduction of the predicted excitonic absorption spectrum (Figure 4 of Bergahäuser *et al.*[3]) with 50 meV linewidths for the A and B excitons. b) Excitonic absorption spectrum from panel (a) with the experimentally determined 70 meV and 110 meV linewidths for the A and B excitons states, respectively. c) Excitonic absorption spectrum from panel (b) but with the step-like broadband background extracted from the PLE data. The black arrow at ~2.36 eV marks the 2S state of the B exciton (as predicted by the model) and clearly demonstrates how the prominence of the peak is significantly diminished due to the broader linewidth.

In Figure S2, we estimate the linewidth of the A and B excitons by fitting our experimental PLE spectrum with the sum of two lorentizian resonances and a sigmoidal step function to approximate the broadband background:

$$I_{PLE}(E) = \frac{1}{E}\sum_{j=A,B}\frac{A_{j,PLE}\gamma_j}{(E-E_j)^2+i\gamma_j^2} + \frac{B}{1+e^{\frac{-(E-E_{cont})}{\gamma_{cont}}}} \quad (1)$$

The terms in the summation, A_j, E_j, and γ_j are the oscillator strength (arbitrary units), resonant energy and linewidth, respectively, of the 1S state of the j (A or B) exciton. The broadband background is approximated by a sigmoidal function with an amplitude of B for $E>E_{\text{cont}}$ and a transition width of γ_{cont}. The optimized values of the fitting parameters are provided in Table S1.

The relative oscillator strengths of the 2S and 3S states, and the relative intensity of the continuum absorption are extracted for the A and B exciton states from Figure 4 of Bergahäuser *et al.*[3] Using these oscillator strengths, the energies for the 1S, 2S, 3S and quasiparticle bandgaps for the A and B excitons from our DFT calculations, the expected absorption spectrum is approximated with the following analytical form:

$$\alpha(E) = \frac{1}{E}\sum_{j=A,B}\left(\sum_{k=1}^{3}\frac{(A_j/C_{j,k})\gamma_j}{(E-E_{j,k})^2+i\gamma_j^2} + \frac{D_y}{1+e^{\frac{E-E_{BG,j}}{0.023\ eV}}}\right) + \frac{B}{1+e^{\frac{E-E_{cont}}{-\gamma_{cont}}}} \quad (2)$$

In the above expression, $C_{j,k}$ is the relative oscillator strength of the k^{th} state (*i.e.*, 1S, 2S or 3S) of the j (A or B) exciton at energy $E_{j,k}$ and $E_{\text{BG},j}$ is the respective bandgap energy. The height of the continuum absorption due to free-carrier excitations for the j exciton is D_j for energies larger than the bandgap and is represented by a sigmoidal function with a transition width 0.023 eV, corresponding to room temperature broadening. The final term incorporates the broadband background extracted from the experimental data. All of the relevant numerical values are provided in Table S1.

The above expression provides a way to analytically demonstrate how the broader, higher-energy exciton transitions of the B exciton can be obscured within the larger ensemble of higher-energy states. Figure S3 plots expression (2) for different linewidth configurations with and without the broadband background extracted from the experimental PLE data.

Table S1 - Numerical values used in the qualitative analysis of linewidth effects. Please note that these values are provided to produce the above curves on their corresponding arbitrary scales and are for qualitative purposes only.

Parameter	Value
A_A	0.13
E_A	1.869 (eV)
γ_A	0.07 (eV)
A_B	0.20
E_B	2.025 (eV)
γ_A	0.11 (eV)
B	0.52
E_{cont}	1.942 (eV)
γ_{cont}	0.066 (eV)

Parameter	Value
$C_{A,1}$	1
$E_{A,1}$	1.88 (eV)
$C_{A,2}$	8.06
$E_{A,2}$	2.21 (eV)
$C_{A,3}$	11.3
$E_{A,3}$	2.28 (eV)
D_A	0.42
$E_{BG,A}$	2.480
$C_{B,1}$	1
$E_{B,1}$	2.036 (eV)
$C_{B,2}$	4.43
$E_{B,2}$	2.365 (eV)
$C_{B,3}$	13.3
$E_{B,3}$	2.430 (eV)
D_B	0.42
$E_{BG,B}$	2.650 (eV)

7. Spatial variations of emission spectra in Figure 2

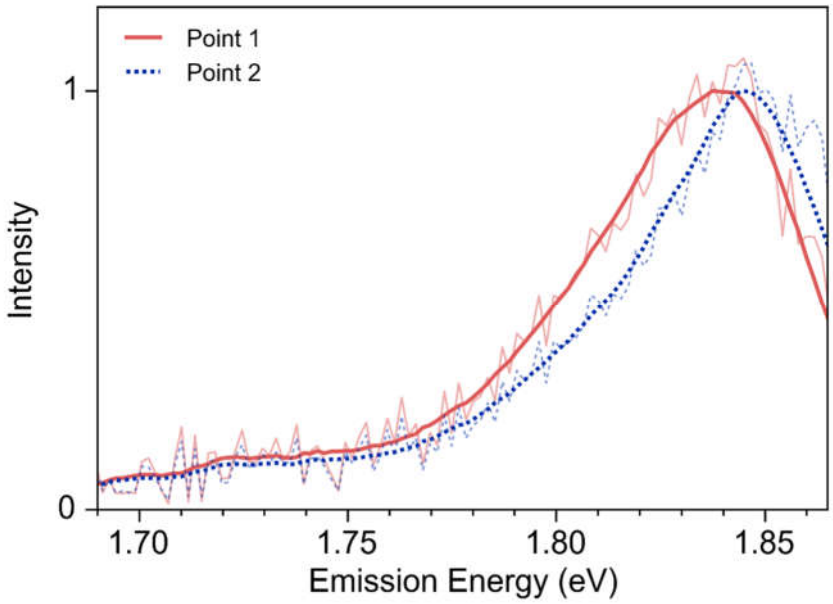

Figure S8 – Emission spectra for points 1 and 2 from Figure 2 of the main text.

8. Fitting analysis for the combined μAbsortion and μPL hyperspectral imaging

Hyperspectral reflectance imaging on single flakes on monolayer MoS_2 were performed by recording spectrum of reflected broadband radiation at normal incidence to the substrate. An objective (100×, 0.95 NA) was used to both provide widefield illumination of the sample and collect the reflected light. A pinhole was used in the detection path to spatially filter the analyzed light to a diffraction-limited region of the sample. The sample was then raster-scanned with respect to the objective and a spectrum of the reflected illumination at each point was acquired. In a similar fashion to previous work[4-5], the spectrum of reflected light from the monolayer MoS_2 was normalized by the spectrum of the reflected light from the bare SiO_2/Si substrate. The same restrained Kramers Kronig analysis of previous work[5] was then applied to the normalized reflectance spectra of each point and used to calculate the local absorption spectrum. We refer to this pervious work for the detailed description of the analysis technique[5]. We also note that within ~500 nm of the edges, scattering effects were observed in the μAbsortion measurements. This peripheral edge was omitted from the this analysis for the sake of simplicity.

Standard confocal μPL hyperspectral imaging was used to image the spatially dependent photoluminescence of the same flake of monolayer MoS_2 with a resolution of ~400 nm. As the μPL and μAbsorption datasets were collected on the same microscope in successive fashion, co-alignment of the datasets was easy and only required a simple spatial transformation to co-align common spatial features such as the vertexes of the flakes. For each spatial position, the photoluminescence spectrum was fitted to three peaks as described in the figure caption. We note that despite over 25 meV shifts in peak positions, the spectra were always best fitted with the three peak configuration illustrated in the figure. This observation leads us to conclude that the low-energy shoulder observed in this dataset is likely due to defects rather than trions.

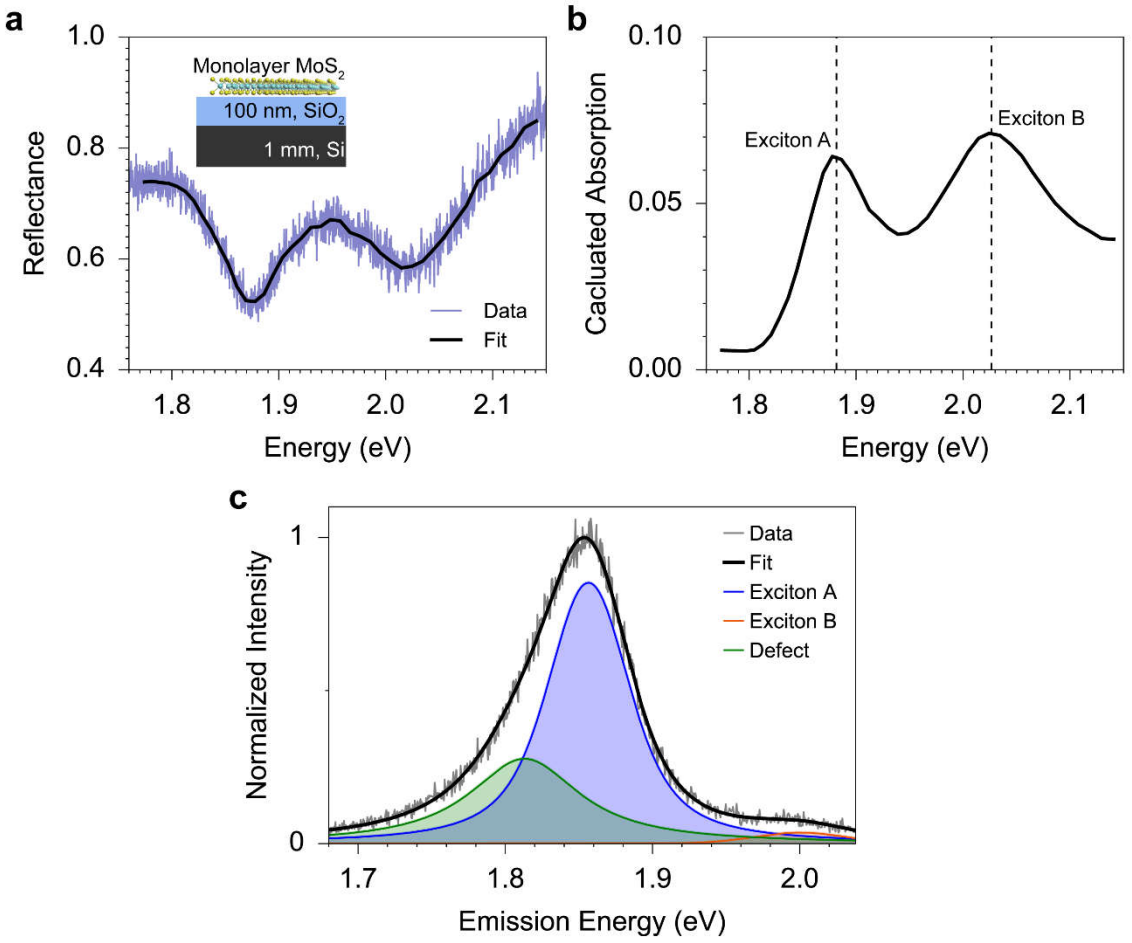

Figure S9 - Fitting analysis used to extract the spatially dependent excitation and emission resonance energies from the hyperspectral μAbsorbtion and μPL measurements shown in the main text. (a) Sample reflectance measurement from a ~400 nm region of monolayer MoS_2. The raw data is shown in blue and the overlaid black line is the fit obtained by applying restrained Kramers-Kronig analysis[5] to the smoothed raw data. Inset is a schematic of the monolayer MoS_2 on the Si/SiO_2 substrate with the corresponding dimension used in the analysis. (b) From the fit to the reflectance data, the local absorption spectrum and be calculated, revealing two distinct peaks that correspond to the A and B exciton states. (c) A sample photoluminescence spectrum from a ~400 nm region of monolayer MoS_2. To fit the spectrum, three Voigt functions were used for the main photoluminescence peak (blue curve), a lower-energy shoulder (green curve) and weak higher-energy hot luminescence from the B exciton (orange curve). The raw data is shown light gray and the overall fit (*i.e.*, the sum of the three peaks) is shown in black.

9. Comparison of Stokes shift data to gate-dependent photoluminescence measurements

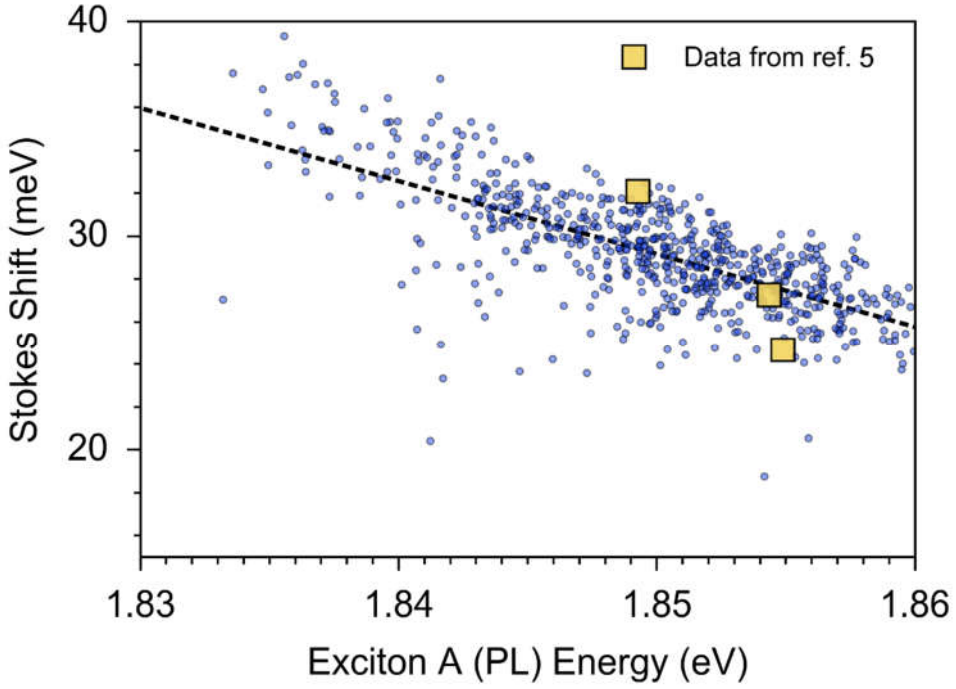

Figure S10 – comparison of correlation between the Stokes shift and exciton energy observed in Figure 4 of the main text to a similar correlation reported by Mak *et al.*[5] Note that the reported values of the exciton energy by Mak *et al.*[5] were taken at 10 K and the data in our work was acquired at room temperature. To correct for the temperature difference, the exciton energies from Mak *et al.*[5], were reduced by 20 meV as determined by comparing their comparison of cryogenic and room temperature PL spectra reported in the same work.

10. Combined optical and Kelvin probe microscopy of a single flake of monolayer MoS_2

To try and identify additional signatures of carrier density fluctuations, scanning Kelvin probe force microscopy (KPFM), which measures nanoscale variations of the work function (or surface potential), was performed in addition to the combined µPL and µAbsorption spectroscopy of a single flake of monolayer MoS_2. Details of the KPFM measurements can be found in previous work[6-7]. Figure S9 shows the co-aligned spatial maps of the excitonic Stokes shift and the surface potential as measured by KPFM. Although variations in the KPFM signal are observed, a correlation between the Stokes shift and surface potential is not observed in these samples. Although these measurements were conducted in an inert N_2 atmosphere, KPFM is ultrasensitive to the surface and the roles of surface contaminants and water layers remains largely unknown, warranting a much more detailed and thorough study before solid conclusions can be reached using such a correlated, multi-modal measurements.

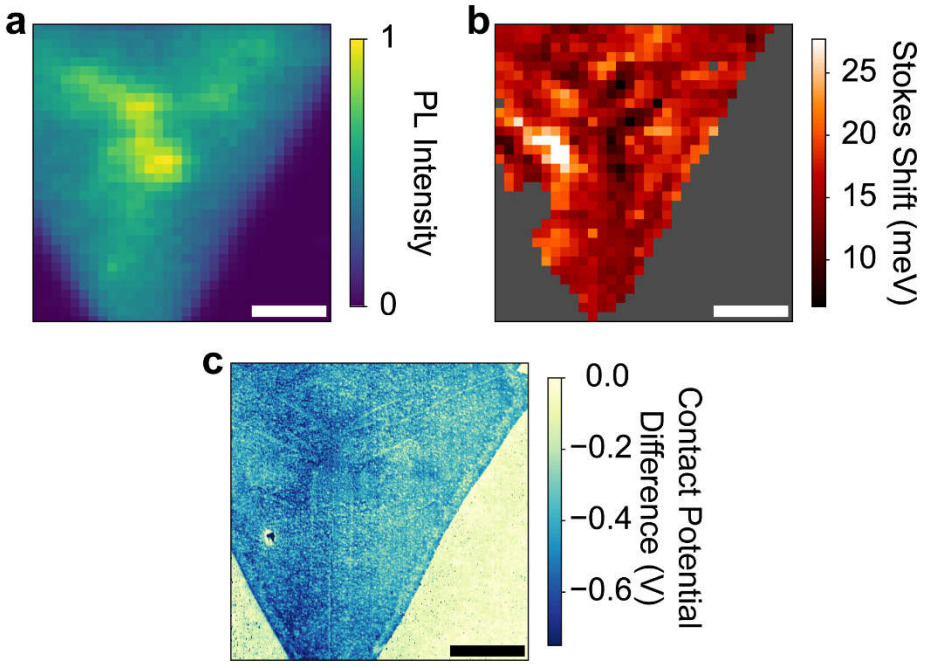

Figure S11 - Combined scanning Kelvin probe force microscopy and combined hyperspectral µPL and µAbsorption imaging of a single flake on monolayer MoS_2. (a) Map of the excitonic emission intensity of a single flake of monolayer MoS_2. (b) The spatial distribution of the measured Stokes shift from the combined µPL and µAbsorption measurements. Note that an ~750 nm border region is omitted from the Stokes shift calculation to avoid the effects of scattering at the edges in the µAbsorption spectroscopy. (c) Surface potential map of the same flake of monolayer MoS_2 acquired using KPFM. Kelvin probe microscopy. Although changes in the surface potential are observed, they do not exhibit a correlation to the spatial variations of the Stokes shift. We suspect that the actual surface potential of the MoS_2 is largely obscured by surface contaminants and/or a water layer. All scale bars are 2 µm.

11. Strain-induced shifts in the exciton energy

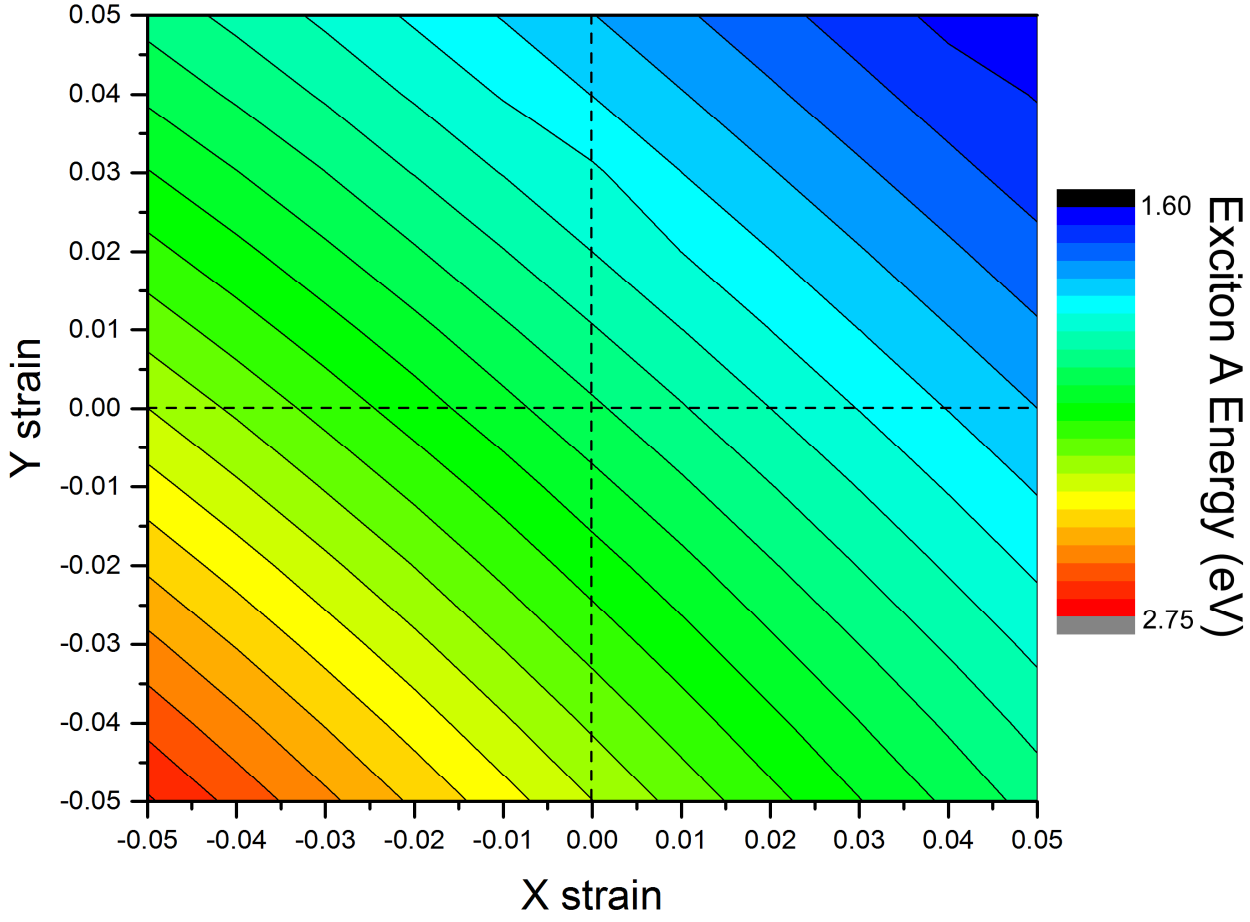

Figure S12 – Strain effects on the energy of exciton A from the excited state calculations described in the main text. A 0.5% strain is sufficient to cause a 20 meV shift in the energy of exciton A.

12. References

1. Kozawa, D.; Kumar, R.; Carvalho, A.; Amara, K. K.; Zhao, W.; Wang, S.; Toh, M.; Ribeiro, R. M.; Castro Neto, A. H.; Matsuda, K.; Eda, G., Photocarrier Relaxation Pathway in Two-Dimensional Semiconducting Transition Metal Dichalcogenides. *Nat. Commun.* **2014,** *5*, 4543.

2. Hill, H. M.; Rigosi, A. F.; Roquelet, C.; Chernikov, A.; Berkelbach, T. C.; Reichman, D. R.; Hybertsen, M. S.; Brus, L. E.; Heinz, T. F., Observation of Excitonic Rydberg States in Monolayer MoS_2 and WS_2 by Photoluminescence Excitation Spectroscopy. *Nano Lett.* **2015,** *15*, 2992-2997.

3. Berghaeuser, G.; Malic, E., Analytical Approach to Excitonic Properties of MoS_2. *Phys. Rev. B: Condens. Matter Mater. Phys.* **2014,** *89*, 125309-125309.

4. Li, Y. L.; Chernikov, A.; Zhang, X.; Rigosi, A.; Hill, H. M.; van der Zande, A. M.; Chenet, D. A.; Shih, E. M.; Hone, J.; Heinz, T. F., Measurement of the Optical Dielectric Function of Monolayer Transition-Metal Dichalcogenides: MoS_2, $MoSe_2$, WS_2, and WSe_2. *Phys. Rev. B: Condens. Matter Mater. Phys.* **2014,** *90*.

5. Mak, K. F.; He, K.; Lee, C.; Lee, G. H.; Hone, J.; Heinz, T. F.; Shan, J., Tightly Bound Trions in Monolayer MoS_2. *Nat. Mater.* **2013,** *12*, 207-211.

6. Zhang, Y. J.; Zherebetskyy, D.; Bronstein, N. D.; Barja, S.; Lichtenstein, L.; Schuppisser, D.; Wang, L. W.; Alivisatos, A. P.; Sameron, M., Charge Percolation Pathways Guided by Defects in Quantum Dot Solids. *Nano Lett.* **2015,** *15*, 3249-3253.

7. Zhang, Y. J.; Ziegler, D.; Salmeron, M., Charge Trapping States at the SiO_2-Oligothiophene Monolayer Interface in Field Effect Transistors Studied by Kelvin Probe Force Microscopy. *ACS Nano* **2013,** *7*, 8258-8265.